RESEARCH ARTICLE

CCCCC pentadentate chelates with planar Möbius aromaticity and unique properties

Congqing Zhu,[1]* Caixia Yang,[2]* Yongheng Wang,[1] Gan Lin,[2] Yuhui Yang,[1] Xiaoyong Wang,[2] Jun Zhu,[1] Xiaoyuan Chen,[3] Xin Lu,[1†] Gang Liu,[2†] Haiping Xia[1†]

The coordinating atoms in polydentate chelates are primarily heteroatoms. We present the first examples of pentadentate chelates with all binding atoms of the chelating agent being carbon atoms, denoted as CCCCC chelates. Having up to five metal-carbon bonds in the equatorial plane has not been previously observed in transition metal chemistry. Density functional theory calculations showed that the planar metallacycle has extended Craig-Möbius aromaticity arising from 12-center–12-electron d_π-p_π π-conjugation. These planar chelates have broad absorption in the ultraviolet-visible–near-infrared region and, thus, notable photothermal performance upon irradiation by an 808-nm laser, indicating that these chelates have potential applications in photothermal therapy. The combination of facile synthesis, high stability, and broad absorption of these complexes could make the polydentate carbon chain a novel building block in coordination chemistry.

INTRODUCTION

Carbon is one of the most fundamental elements in chemistry. However, the coordinating atoms in polydentate chelates are mainly occupied by a variety of donor heteroatoms, of which N, P, O, and S are common examples (1–4). Examples of polydentate chelates with carbon exclusively as binding atoms have proven to be much more difficult to realize (5–12). Even tridentate CCC-type pincer complexes are limited, and almost all contain an N-heterocyclic carbene unit, which is also a two-electron donor analogous to heteroatoms (13–15). To our knowledge, a pentadentate chelate with all-carbon ligating atoms has not been previously reported. Furthermore, Möbius aromatics, especially planar Craig-type Möbius aromatic species with $4n$ mobile electrons ($4ne$), have proven to be particularly difficult to synthesize. Although this concept was originally proposed in 1958 based on planar delocalized systems with $4ne$ d_π-p_π π-conjugation (16), 8 years earlier than twisted Heilbronner-type Möbius aromaticity (17–23), examples of planar Craig-type Möbius aromaticity are very rare and, to date, are limited to metallapentalenes/metallapentalynes that have eight-center–eight-electron (8c-8e) d_π-p_π π-conjugation (6, 7).

Here, we report the first CCCCC pentadentate chelates, in which all of the five coordinated carbons lie in the equatorial plane. These structures represent the highest carbon coordination number for a metal atom in a planar geometry. We demonstrate that these conjugated chelates exhibit excellent thermodynamic stability and broad absorption from the ultraviolet-visible (UV-vis) to the near-infrared (NIR) region. A detailed density functional theory (DFT) study shows that these complexes have extended Craig-type Möbius aromaticity arising from planar 12-center–12-electron (12c-12e) d_π-p_π π-conjugation within

their equatorial fused ring, which is the largest planar Möbius aromatic system synthesized to date. In addition, the broad absorption in the NIR region makes these novel pentadentate carbon chain chelates useful photothermal therapy (PTT) agents.

RESULTS AND DISCUSSION

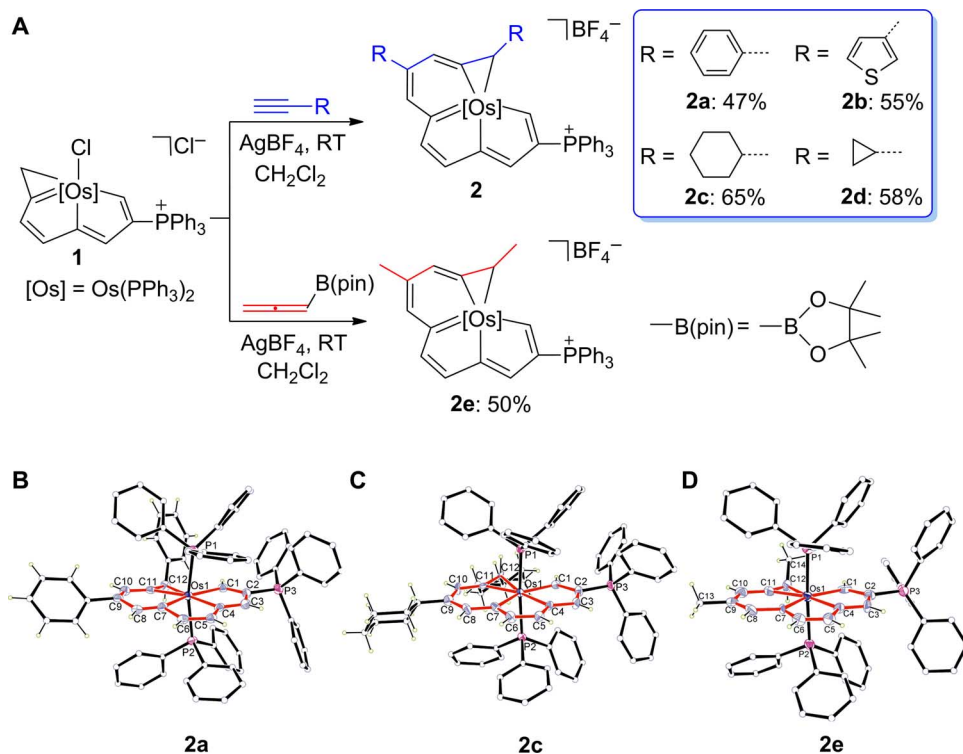### Synthesis and structural characterization

In the presence of $AgBF_4$, treatment of complex **1** (9) with phenylacetylene (PhC≡CH) at room temperature for 2 hours led to the formation of **2a** (Fig. 1A). Complex **2a** exhibits excellent thermal stability both in solution and in the solid state. For instance, the solid sample of **2a** was stable even when exposed to air at room temperature for 1 year or when heated at 150°C in air for 3 hours. The molecular structure of **2a** was confirmed by x-ray diffraction (Fig. 1B), with the osmium center adopting a slightly distorted pentagonal bipyramidal geometry. All five coordination sites in the equatorial plane are occupied by carbon atoms, and the axial positions are occupied by two phosphorus atoms. Note that this system contains five metal-carbon bonds in the equatorial plane, which has not been previously observed in coordination chemistry. The maximum carbon coordination number for a transition metal in a planar geometry is previously four (10). Therefore, complex **2a** represents the highest carbon coordination number in planar metallacycles known to date.

The metallacyclic unit in **2a** is almost coplanar, as reflected by the small mean deviation from the least-squares plane (0.0523 Å). Structurally, complex **2a** is constituted by a 12-atom carbon chain (C1–C12) as a pentadentate ligand chelating to a central transition-metal atom (Os). The sum of the angles in the fused five-membered rings (5MRs) and the 6MR are 540.1°, 540.0°, and 719.7°, which are close to the ideal values of 540° and 720°. The bond distances of Os1–C1 (2.088 Å), Os1–C4 (2.107 Å), Os1–C7 (2.090 Å), and Os1–C11 (2.025 Å) are within the range of those of osmapentalene (1.926 to 2.139 Å) reported previously (7), indicating the delocalized metal-carbon bonds. The Os1–C12 (2.253 Å) bond distance is similar to that of the Os–C(sp^3) bond in complex **1** (2.272 Å) (9).

Zhu et al. Sci. Adv. 2016;2:e1601031   26 August 2016

1 of 7

Fig. 1. Syntheses and x-ray molecular structures of pentadentate carbon chain chelates. (**A**) Ring expansion reactions of complex **1** with alkynes or allene, leading to the formation of **2a** to **2e**. (**B** to **D**) X-ray molecular structures of the cations of **2a** (B), **2c** (C), and **2e** (D) drawn with 50% probability (the protons in PPh₃ are omitted for clarity). RT, room temperature.

The molecular structure of **2a** was further confirmed by nuclear magnetic resonance (NMR) spectroscopy, high-resolution mass spectrometry (HRMS), and elemental analysis. A doublet signal at 13.22 parts per million (ppm) in the ^{1}H NMR spectrum is assigned to the H1 proton, which is shifted slightly downfield compared to those in the spectra of osmapentalene (11.94 to 12.46 ppm) (7). The signals of other protons on the fused 5MRs and 6MR are observed in the aromatic region (8.71 to 7.55 ppm). In the ^{31}P NMR spectrum, the CPPh₃ signal appears at 9.24 ppm, and two OsPPh₃ signals appear at −8.45 and −19.22 ppm. The ^{13}C NMR spectrum of **2a** displays metal-bonded carbon atoms in the typical downfield regions for C1 (208.0 ppm), C4 (200.8 ppm), C7 (232.0 ppm), and C11 (218.7 ppm) and an upfield signal for C12 (14.9 ppm), as expected for sp^3 hybridization.

A plausible mechanism for this ring expansion reaction is proposed in fig. S1. To explore the scope of this protocol, we treated a variety of alkynes with complex **1** (Fig. 1A). The reactions of **1** with 3-ethynylthiophene, ethynylcyclohexane, or ethynylcyclopropane afforded the expected products **2b**, **2c**, and **2d**, respectively. All of these complexes were characterized by multidimensional NMR spectra, HRMS, and elemental analysis. The structural features of **2c** are essentially identical to those observed for **2a**, as confirmed by single-crystal x-ray diffraction (Fig. 1C).

Notably, this reaction is not limited to alkynes; allene is also an effective reagent to form the ring-expanded product **2e**. For the synthesis of **2e**, complex **1** was reacted with allenylboronic acid pinacol ester in the presence of AgBF₄ at room temperature for 12 hours (Fig. 1A). The molecular structure of **2e** was confirmed by NMR spectroscopy, HRMS, and elemental analysis, as well as by single-crystal x-ray

diffraction (Fig. 1D). The most notable structural feature of **2e** is the planarity of the metallacycle, as reflected by the small mean deviation from the least-squares plane (0.0345 Å) and by the sum of the angles in the fused 5MRs (539.9°) and the 6MR (719.9°). The pentagonal bipyramidal geometry, Os–C bond distances, and proton chemical shift for **2e** are similar to those for **2a**. Therefore, through the reactions of **1** with alkynes or allene, a series of previously undescribed pentadentate chelates were constructed with a 12-atom carbon chain (C1–C12) and an osmium center (with axial PPh₃ ligands).

These structures prompted us to reexamine the scope of the pincer complexes. Traditionally, the term "pincer" has been used to describe planar tridentate ligands (**I**) (24, 25). The analogous planar tetradentate (**II**) and pentadentate (**III**) chelates, such as metalloporphyrin and complex **2**, can be included in the family of pincer or pincer-type complexes.

DFT calculations

To elucidate the bonding and electronic structure of these unique pentadentate carbon chain chelates, we performed DFT calculations on simplified unsubstituted models of **2′** by replacing the PPh₃ ligands with PH₃ groups. The DFT-optimized structural parameters of **2′**, especially the bond distances in the metallacycle, agree well with those observed for the crystal structure of **2a**. The calculated Wiberg bond indices for the Os–C bonds in **2′** are 0.88, 0.72, 0.87, 0.73, and 0.62 for Os1–C1, Os1–C4, Os1–C7, Os1–C11, and Os1–C12, respectively, indicating strongly covalent Os–C bonding between the osmium center and these carbons, as depicted in the resonance structures (fig. S2). The pentadentate CCCCC chelate formed by the 12-atom carbon chain with the osmium center exhibits aromatic character,

which was confirmed by experimental observations (for example, high stability, perfect planarity, and downfield proton chemical shift) and DFT calculations.

The isomerization stabilization energy (ISE) (26) was computed to evaluate the π-aromaticity of **2′**. The ISE values for the fused 5MRs and the 6MR are −8.9, −16.2, and −6.3 kcal mol^{-1} (fig. S3). The sum of these values (−31.4 kcal mol^{-1}) is close to the global ISE value (−29.0 kcal mol^{-1}) of **2′**, indicating that such carbon chain chelates benefit from extra stability arising from quite strong 12c-12e d$_\pi$-p$_\pi$ π-conjugation. Note that the global ISE value of **2′** is comparable to that computed for the osmapentalene (−31.4 kcal mol^{-1}) (7), which has planar Craig-type Möbius aromaticity pertaining to its 4ne (8c-8e) d$_\pi$-p$_\pi$ π-conjugation.

To probe the nature of the aromaticity in complex **2′**, we first analyzed its electronic structure. The seven-coordinated Os center has three electrons in its two unhybridized d$_\pi$ atomic orbitals (AOs), and the 11-center carbon chain ligand contributes 11 electrons. These π-AOs constitute seven occupied π-MOs of **2′**, as shown in fig. S4. Among them, six key occupied π-MOs selected in Fig. 2 reflect the π-delocalization along the perimeter of the tricyclic system, which are jointly responsible for the planar 4ne (12c-12e) d$_\pi$-p$_\pi$ π-conjugation of Craig-type Möbius aromaticity (16, 27).

The aromaticity in the model complex **2′** was further confirmed by the anisotropy of the current-induced density (ACID) calculations (28). The ACID method is a versatile, intuitive, and generally applicable approach to investigating and visualizing electron delocalization. The clockwise ring current in the π-system is displayed along the periphery of the fused 5MRs and the 6MR, indicating the π-aromaticity (Fig. 3A and fig. S5). The current-density vectors plotted on the ACID isosurface of the σ-system indicate a diatropic ring current only in the 3MR, suggesting the σ-aromaticity in the 3MR of **2′** (Fig. 3B and fig. S6).

The σ-aromaticity in the 3MR of **2′** was further examined by canonical MO (CMO) nucleus-independent chemical shift (NICS) calculations (fig. S4) (29, 30). The results reveal that the total contribution of the NICS(1)$_{zz}$ value (−38.3 ppm) for the 3MR from all the σ orbitals is more negative than that (−23.5 ppm) from all the σ and π orbitals, showing σ-aromaticity in the 3MR, as previously observed in the reactant, complex **1** (9). The NICS(1)$_{zz}$ values for the fused 5MRs and the 6MR from all occupied MOs are −27.9, −16.7, and −6.8 ppm,
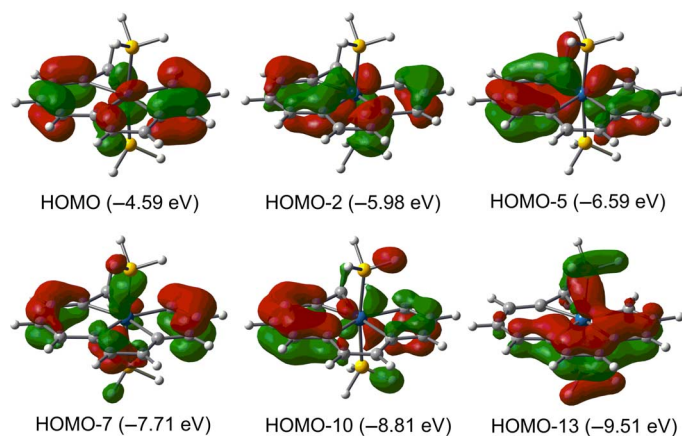
indicating aromaticity in these rings. Thus, the nature of the aromaticity in complex **2′** could be considered as a combination of Craig-type Möbius aromaticity with σ-aromaticity. Overall, the ISE values, in conjunction with the ACID analysis and NICS calculations, unambiguously confirm the aromaticity, which is critical in stabilizing these planar pentadentate CCCCC chelating structure.
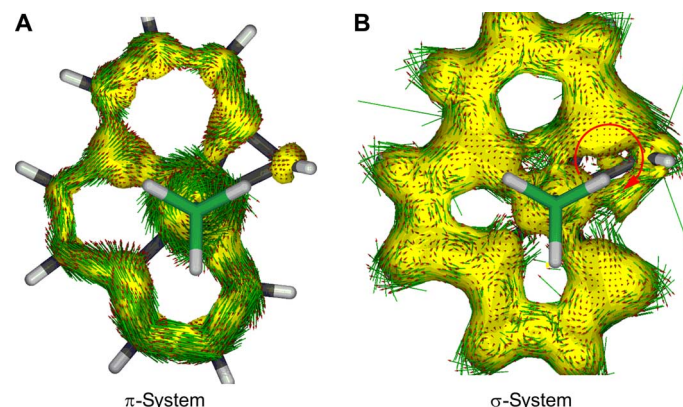
UV-vis–NIR absorption spectra

All complexes, **2a** to **2e**, exhibit a broad absorption band in the UV-vis–NIR region (Fig. 4). The absorption maxima of **2a** and **2b** in low-energy absorption bands are 810 nm (logε = 2.53, ε is the molar absorption coefficient in M^{-1} cm^{-1}) and 805 nm (logε = 2.48), respectively. The absorption maxima of **2c** to **2e** in the low-energy absorption regions are blue-shifted to 740 nm. These results indicate that the photophysical properties of these novel pentadentate carbon chain chelates can be effectively modulated by structural modifications.

To understand the NIR absorption spectra, we carried out time-dependent DFT (TD-DFT) calculations on the cations of **2a** and **2c**. The lowest unoccupied MO (LUMO) level of **2a** delocalized over its aryl substituent is 0.21 eV lower than that of **2c**, and the highest occupied MO (HOMO) levels of **2a** and **2c** are similar (fig. S7). These results suggest that the aryl substituents on the metallacycle lower the LUMO levels substantially but have a small effect on the HOMO levels. The theoretical spectra are consistent with the trends of the experimental spectra. Specifically, the observed absorption bands (around 810 nm for complex **2a** and around 740 nm for **2c**) can be ascribed to their HOMO→LUMO transitions.

PTT in vitro and in vivo

PTT usually uses NIR light-absorbing agents to generate heat from energy, leading to the thermal ablation of cancer cells (31). Because of the broad absorbance spectra in the NIR region, the photothermal effect of these pentadentate carbon chain chelates was first examined by measuring the temperature increase of various concentrations of **2a** under NIR laser (808 nm, 1 W cm^{-2}) radiation. As shown in Fig. 5A, the temperature of the water-ethanol solution (95% v/v) containing

Fig. 2. Six key occupied perimeter π molecular orbitals (π-MOs) of the model complex 2′. The eigenvalues of the MOs are given in parentheses.

HOMO (−4.59 eV)   HOMO-2 (−5.98 eV)   HOMO-5 (−6.59 eV)

HOMO-7 (−7.71 eV)   HOMO-10 (−8.81 eV)   HOMO-13 (−9.51 eV)

Fig. 3. ACID isosurfaces of the model complex 2′ separated into the π- and σ-contribution. Current-density vectors are plotted onto the ACID isosurface of 0.035. (**A** and **B**) The diatropic ring current displayed in the periphery of the 6MR and the fused 5MRs indicates the π-aromaticity (A), whereas the diatropic ring current only exists in the 3MR, indicating the σ-aromaticity (B). The magnetic field vector is orthogonal with respect to the ring plane and points upward (clockwise currents are diatropic).

π-System   σ-System
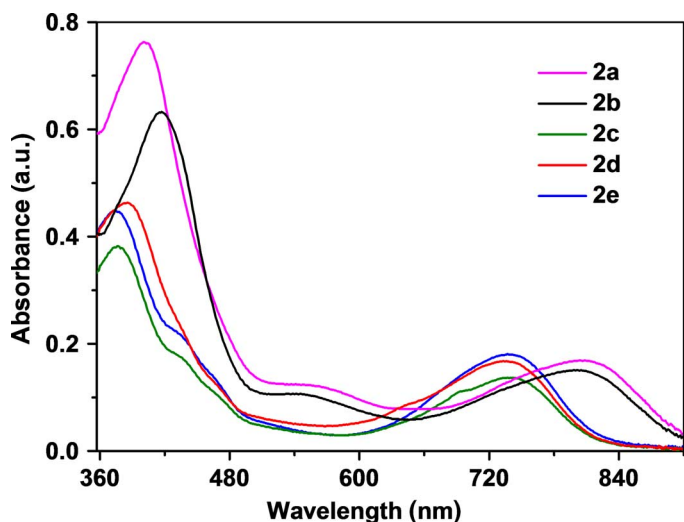
Fig. 4. UV-vis–NIR absorption spectra of 2a to 2e (5.0 × 10⁻⁵ M) measured in CH₂Cl₂ at room temperature. The low-energy absorption bands of **2a** and **2b** are clearly red-shifted compared to those of **2c** to **2e**, suggesting enhanced π-conjugation of the metallacycle from the introduction of aryl substituents. a.u., arbitrary units.

complex **2a** (0.1 mg ml⁻¹) significantly increased from 28° to 52°C within 5 min, whereas the solvent (without complex **2a**) exhibited a negligible temperature change (less than 3°C) under similar conditions. Because of the strong d_π-p_π π-conjugation between the osmium center and the 12-atom carbon chain, **2a** exhibited good photothermal stability under the laser irradiation conditions (fig. S8). The photothermal effect of **2b** was similar to that of **2a**, which is more preferable than that of reported organometallics (10). These results suggest that these chelates have potential applications in PTT.

PTT often requires preferential tumor accumulation of these photo-absorbing agents to reach sufficient hyperthermia. Generally, amphiphilic polymers serve as useful nanocarriers with high clinical translational potential for loading and delivering hydrophilic compounds, and polyethylene glycol (PEG) has widely emerged as a powerful coating for nanoparticles to achieve a long circulation time and high accumulation in the tumor via the enhanced permeability and retention effects (32–34). Here, the amphiphilic polymer alkyl–polyethylenimine (PEI)₂ₖ–PEG₂ₖ (35, 36) was prepared and used for the solubilization of complex **2a**. Transmission electron microscopy (TEM) image and dynamic light scattering (DLS) data showed that the complex **2a**–loaded micelles (**2a@NPs**) were well dispersed in water, with an average diameter of approximately 70 nm (fig. S9). Formulation of **2a** with a large loading capacity (61.2 weight percent), high water solubility, good photothermal activity, and biocompatibility was achieved by generating **2a@NPs** for cancer PTT applications (figs. S10 and S11). As expected, SCC7 cells (a squamous cell carcinoma cell line) with **2a@NPs** clearly exhibited lower cell viability under
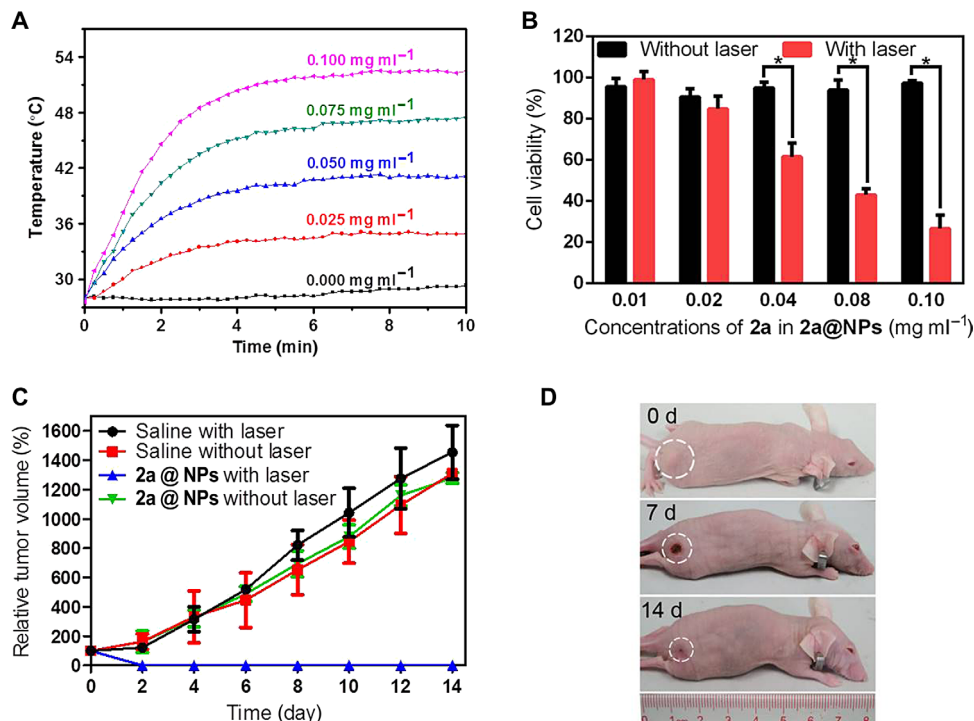
Fig. 5. Photothermal therapy. (A) Temperature elevation of solvent and the solutions of **2a** at different concentrations upon laser irradiation. **(B)** Cell viability of SCC7 cells exposed to **2a@NPs** without or with laser irradiation. Cells incubated with **2a** (0.10 mg ml⁻¹) in **2a@NPs** exhibited approximately 26% cell viability after NIR laser irradiation for 5 min. **(C)** Tumor growth curves after PTT treatment. **(D)** Photographs of the SCC7 tumor–bearing mice 0, 7, and 14 days after PTT treatment with **2a@NPs**. Scale bar, 50 nm. Error bars in (B) and (C) represent SDs (laser intensity: λ = 808 nm, 1 W cm⁻²).

laser irradiation as compared to control experiments without laser irradiation (Fig. 5B).

Because **2a@NPs** exhibited excellent tumor accumulation (fig. S12) and photothermal performance in vivo after intravenous injection (fig. S13), we investigated the feasibility of using **2a@NPs** as a PTT reagent for tumor ablation in vivo. SCC7 tumor–bearing mice were randomly divided into four groups (five mice per group): a group with saline injection and NIR laser irradiation, a group with only saline injection, a group treated with **2a@NPs** plus NIR laser irradiation, and a group treated with only **2a@NPs**. As shown in Fig. 5C, the tumor volumes of the control experiment increased exponentially and were up to 12 times larger at day 14 than those at day 1; however, the group of mice that received both intravenous injection and irradiation of **2a@NP** showed tumor ablation 2 days after treatment and exhibited thorough regression of the tumor in 14 days (Fig. 5, C and D). To the best of our knowledge, this work represents the first example of organometallics used for PTT; this treatment showed comparable efficacy to that reported for carbon nanotubes and nanoporphyrin (37, 38). Therefore, our results clearly demonstrate that **2a@NP** is effective for cancer PTT, although the long-term toxicity should be investigated before clinical translation.

CONCLUSION

Here, we have demonstrated the CCCCC pentadentate chelates with the highest carbon coordination number for a metal atom, which were formed by the coordination of a 12-atom carbon chain (carbolong) to a transition metal. The presence of as many as five binding carbon atoms in the equatorial plane is unprecedented. This result extends our perception of the chelating ability of carbon chain. Thus, the concept of the pincer complex can be extended from tridentate to planar polydentate chelates. Furthermore, these CCCCC pentadentate chelates are manifested to have rare extended Craig-type Möbius aromaticity and show broad absorption spectra in the UV-vis–NIR region. Overall, because of their facile syntheses, high thermodynamic stability, broad absorption spectra, and significant photothermal properties, these novel pentadentate carbon chain chelates provide a promising material for biomedicine and solar energy utilization.

MATERIALS AND METHODS

General considerations

All syntheses were carried out under an inert atmosphere (N_2) using standard Schlenk techniques unless otherwise stated. Solvents were distilled from sodium/benzophenone (hexane and diethyl ether) or calcium hydride (dichloromethane) under N_2 before use. The metal-lapentalene derivate **1** was synthesized according to a previously published procedure, Zhu et al. (9). Other reagents were used as received from commercial sources without further purification. Column chromatography was performed on alumina gel (200 to 300 mesh) in air. NMR spectroscopic experiments were performed on a Bruker AVIII-500 (^{1}H, 500.1 MHz; ^{13}C, 125.8 MHz; ^{31}P, 202.5 MHz) spectrometer at room temperature. ^{1}H and ^{13}C NMR chemical shifts (δ) are relative to tetramethylsilane, and ^{31}P NMR chemical shifts are relative to 85% H_3PO_4. The absolute values of the coupling constants are given in hertz. Multiplicities are abbreviated as singlet (s), doublet (d), triplet (t),

multiplet (m), and broad (br). HRMS experiments were conducted on a Bruker En Apex Ultra 7.0T FT-MS. Elemental analyses were performed on a Vario EL III elemental analyzer. Absorption spectra were recorded on a Shimadzu UV2550 UV-vis spectrophotometer. The synthetic details given here for **2a** was representative of all the compounds described. Further experimental details and the synthesis procedures for **2b** to **2e** are described in the Supplementary Materials.

Synthesis of 2a

Phenylacetylene (93 μl, 0.85 mmol) was added to a mixture of complex **1** (200 mg, 0.17 mmol) and $AgBF_4$ (100 mg, 0.51 mmol) in dichloromethane (10 ml). The reaction mixture was stirred at room temperature for 2 hours to yield a yellow-green solution, and then the solid suspension was removed by filtration. The filtrate was reduced under vacuum to approximately 2 ml and then purified by column chromatography (neutral alumina, eluent: dichloromethane/methanol = 20:1) to give a green solution. The green solid of compound **2a** (110 mg, 47%) was collected after the solvent was evaporated to dryness under vacuum, and the resulting residue was washed with diethyl ether and then dried under vacuum. ^{1}H NMR plus ^{1}H-^{13}C HSQC (500.1 MHz, CD_2Cl_2): δ = 13.22 (d, J_{P-H} = 21.1 Hz, 1H, H1), 8.71 (s, 1H, H3), 8.12 (s, 1H, H8), 7.76 (s, 1H, H10), 7.63 (s, 1H, H5), 7.55 (s, 1H, H6), 6.73 (dd, J_{P-H} = 13.8, 2.5 Hz, 1H, H12), 8.10–5.78 ppm (m, 55H, other aromatic protons). ^{31}P NMR (202.5 MHz, CD_2Cl_2): δ = 9.24 (t, J_{P-P} = 6.7 Hz, CPPh$_3$), −8.45 (dd, J_{P-P} = 254.7 Hz, J_{P-P} = 6.7 Hz, OsPPh$_3$), −19.22 (dd, J_{P-P} = 254.7 Hz, J_{P-P} = 6.7 Hz, OsPPh$_3$). ^{13}C NMR plus DEPT-135, ^{1}H-^{13}C HMBC, and ^{1}H-^{13}C HSQC (125.8 MHz, CD_2Cl_2): δ = 232.0 (s, C7), 218.7 (s, C11), 208.0 (br, C1), 200.8 (d, J_{P-C} = 25.7 Hz, C4), 163.4 (s, C6), 159.2 (s, C5), 159.1 (s, C9), 136.6 (d, J_{P-C} = 25.3 Hz, C3), 128.6 (s, C8), 120.7 (d, J_{P-C} = 87.1 Hz, C2), 114.4 (s, C10), 14.9 (s, C12), 148.4 (s, Ph), 142.7 (s, Ph), 134.4–124.6 ppm (m, other aromatic carbons). HRMS (ESI): mass/charge ratio (m/z) calcd for $[C_{78}H_{62}OsP_3]^+$, 1283.3683; found, 1283.3680. Anal. calcd (%) for $C_{78}H_{62}OsP_3BF_4$: C 68.42, H 4.56; found: C 68.62, H 4.77.

Preparation of 2a@NPs. The **2a@NPs** were prepared according to the method described in a previous report, Liu et al. (35), with some modifications. Briefly, PEG_{2k} was activated with N,N'-carbonyldiimidazole in tetrahydrofuran and reacted with alkyl-PEI_{2k} for 24 hours at room temperature. The product (alkyl-PEI_{2k}-PEG_{2k}) was obtained after precipitation in cold ether and dialysis against water to remove the residue PEG. Then, **2a** was mixed with alkyl-PEI_{2k}-PEG_{2k} in chloroform. The mixed solutions were added to distilled water dropwise under sonication, and the resulting solution was shaken overnight. Subsequently, the residual chloroform was removed by rotary evaporation to obtain the **2a@NPs**.

In vitro cytotoxicity

The cells were maintained in Dulbecco's modified Eagle's medium containing 10% fetal bovine serum and 1% streptomycin/ampicillin at 37°C with 5% CO_2. To confirm the cytotoxicity of the **2a@NPs**, 3-(4,5-dimethylthiazol-2-yl)-2,5-diphenyltetrazolium bromide (MTT) assays were conducted on SCC7, SCG79011, and 4T1 cell lines following incubation with **2a@NPs** (**2a** concentration: 0.10, 0.20, 0.40, 0.80, and 0.10 mg ml^{-1}) for 5 hours (39, 40). We observed that **2a@NPs** exhibited low cell cytotoxicity on SCC7, SCG79011, and 4T1 cancer cells (fig. S11), suggesting that **2a@NPs** have good biocompatibility. For photothermal injury, the SCC7 cells were incubated with **2a@NPs** for 5 hours, and the medium was replaced with fresh medium, irradiated

with an 808-nm NIR laser (1 W cm^{-2}) for 10 min, and then incubated overnight before being subjected to the standard MTT assay.

In vivo efficacy

Female BALB/c nude mice (18 to 20 g) were used under protocols approved by the Xiamen University Laboratory Animal Center. For the SCC7 carcinoma model, about 5×10^6 SCC7 cells in 50 μl of phosphate-buffered saline were injected subcutaneously into the hind flank of mice. The mice were used when the tumor volumes reached 50 to 60 mm^3. To demonstrate the tumor biodistribution behavior of **2a@NPs**, dynamic IR thermal images were obtained (fig. S12A). **2a@NPs** (**2a**: 10 mg kg^{-1}) were intravenously injected into the tumor-bearing mice, the tumors were irradiated with an 808-nm NIR laser (1 W cm^{-2}) for 10 min, and the temperature curves were recorded at 1, 3, 5, 7, and 10 hours after injection. The biodistribution of **2a@NPs** at various tissues was carried out using inductively coupled plasma MS (ICP-MS). The organs (including heart, liver, spleen, lung, and kidney) and tumors were extracted at 5 hours after injection. Each tissue was further treated with 2.0 ml of aqua regia for 48 hours until all the tissues were digested in the solutions. The distribution of **2a@NPs** at various tissues was calculated according to the concentration of Os from **2a@NPs** measured by ICP-MS (fig. S12B).

For PTT, SCC7 tumor–bearing mice were intravenously injected with **2a@NPs** (**2a**: 10 mg kg^{-1}), and the tumors were photoirradiated for 10 min (1 W cm^{-2}) at 5 hours after injection. To monitor the PTT efficiency, the tumor volumes were measured every other day for 2 weeks (*39*, *40*). The following equation was used to monitor the volume change of tumors: tumor volume = length × width^2/2. In the equation, length is the largest diameter, and width is the smallest diameter. The body weights of the mice in all groups showed no obvious decrease, suggesting low toxicity of all treatments (fig. S14). Experimental results are means ± SD. Statistical analysis was performed using Student's *t* test. *$P < 0.05$ was considered statistically significant.

X-ray crystallographic analysis

All single crystals suitable for x-ray diffraction were grown from a dichloromethane solution layered with hexane. Single-crystal x-ray diffraction data were collected at 173 K on a Rigaku R-AXIS SPIDER IP CCD (charge-coupled device) area detector using graphite-monochromated Mo Kα radiation (λ = 0.71073 Å). Semiempirical or multiscan absorption corrections (SADABS) were applied (*41*). All structures were solved by the Patterson function, completed by subsequent difference Fourier map calculations, and refined by full-matrix least squares on F^2 using the SHELXTL program package (*42*). All nonhydrogen atoms were refined isotropically unless otherwise stated. Hydrogen atoms were placed at idealized positions and assumed the riding model. Crystal data and structure refinement for **2a**, **2c**, and **2e** are given in table S1. All of the x-ray molecular structures, selected bond distances (in angstroms), and angles (in degrees) can be found in figs. S15 to S17.

Computational details

All structures were optimized at the B3LYP level of DFT (*43*–*45*). In addition, frequency calculations were performed to confirm the characteristics of the calculated structures as minima. In the B3LYP calculations, the effective core potentials of Hay and Wadt with a double-ζ valence basis set (LanL2DZ) were used to describe the Os and P atoms, whereas the standard 6-311++G(d,p) basis set was used for the C and H atoms (*46*). Polarization functions were added for Os [ζ(f) = 0.886], Cl [ζ(d) = 0.514], and P [ζ(d) = 0.34] (*47*) in all calculations. NICS values were calculated at the B3LYP-GIAO/6-311++G(d,p) level. All of the optimizations were performed with the Gaussian 09 software package (*48*). To understand the absorption spectra, we performed TD-DFT calculations on **2a** and **2c** at the BLYP/6-31G (d) level (*49*). In TD-DFT calculations, the structures were extracted from x-ray diffraction data, and the polarizable continuum model was used, with dichloromethane as the solvent (*50*). The CMO-NICS calculations were carried out with the NBO 5.0 program (*30*), and the ACID calculations were carried out with the ACID program (*28*). See data file S1 for the Cartesian coordinates.

REFERENCES AND NOTES

1. T. R. Cook, P. J. Stang, Recent developments in the preparation and chemistry of metalla-cycles and metallacages via coordination. *Chem. Rev.* **115**, 7001–7045 (2015).
2. H. I. Karunadasa, E. Montalvo, Y. Sun, M. Majda, J. R. Long, C. J. Chang, A molecular MoS$_2$ edge site mimic for catalytic hydrogen generation. *Science* **335**, 698–702 (2012).
3. H. I. Karunadasa, C. J. Chang, J. R. Long, A molecular molybdenum-oxo catalyst for generating hydrogen from water. *Nature* **464**, 1329–1333 (2010).
4. M. Albrecht, M. Lutz, A. L. Spek, G. van Koten, Organoplatinum crystals for gas-triggered switches. *Nature* **406**, 970–974 (2000).
5. A. Sattler, G. Parkin, A new class of transition metal pincer ligand: Tantalum complexes that feature a [CCC] X$_3$-donor array derived from a terphenyl ligand. *J. Am. Chem. Soc.* **134**, 2355–2366 (2012).
6. C. Zhu, S. Li, M. Luo, X. Zhou, Y. Niu, M. Lin, J. Zhu, Z. Cao, X. Lu, T. Wen, Z. Xie, P. R. Schleyer, H. Xia, Stabilization of anti-aromatic and strained five-membered rings with a transition metal. *Nat. Chem.* **5**, 698–703 (2013).
7. C. Zhu, M. Luo, Q. Zhu, J. Zhu, P. R. Schleyer, J. I.-C. Wu, X. Lu, H. Xia, Planar Möbius aromatic pentalenes incorporating 16 and 18 valence electron osmiums. *Nat. Commun.* **5**, 3265 (2014).
8. C. Zhu, Y. Yang, M. Wu, M. Luo, J. Fan, J. Zhu, H. Xia, Five-membered cyclic metal carbyne: Synthesis of osmapentalynes by the reactions of osmapentalene with allene, alkyne, and alkene. *Angew. Chem. Int. Ed.* **54**, 7189–7192 (2015).
9. C. Zhu, X. Zhou, H. Xing, K. An, J. Zhu, H. Xia, σ-Aromaticity in an unsaturated ring: Osmapentalene derivatives containing a metallacyclopropene unit. *Angew. Chem. Int. Ed.* **54**, 3102–3106 (2015).

10. C. Zhu, Y. Yang, M. Luo, C. Yang, J. Wu, L. Chen, G. Liu, T. Wen, J. Zhu, H. Xia, Stabilizing two classical antiaromatic frameworks: Demonstration of photoacoustic imaging and the photothermal effect in metalla-aromatics. *Angew. Chem. Int. Ed.* **54**, 6181–6185 (2015).

11. C. Zhu, Q. Zhu, J. Fan, J. Zhu, X. He, X.-Y. Cao, H. Xia, A metal-bridged tricyclic aromatic system: Synthesis of osmium polycyclic aromatic complexes. *Angew. Chem. Int. Ed.* **53**, 6232–6236 (2014).

12. A. D. McNaught, A. Wilkinson, *IUPAC: Compendium of Chemical Terminology, The "Gold Book"* (Blackwell Scientific Publications, Oxford, ed. 2, 1997).

13. J. Navarro, O. Torres, M. Martín, E. Sola, Iridium complexes of the doubly cyclometalated NHC ligand IMes". *J. Am. Chem. Soc.* **133**, 9738–9740 (2011).

14. R. G. Alabau, B. Eguillor, J. Esler, M. A. Esteruelas, M. Oliván, E. Oñate, J.-Y. Tsai, C. Xia, CCC–pincer–NHC osmium complexes: New types of blue-green emissive neutral compounds for organic light-emitting devices (OLEDs). *Organometallics* **33**, 5582–5596 (2014).

15. E. B. Bauer, G. T. S. Andavan, T. K. Hollis, R. J. Rubio, J. Cho, G. R. Kuchenbeiser, T. R. Helgert, C. S. Letko, F. S. Tham, Air- and water-stable catalysts for hydroamination/cyclization. Synthesis and application of CCC–NHC pincer complexes of Rh and Ir. *Org. Lett.* **10**, 1175–1178 (2008).

16. D. P. Craig, N. L. Paddock, A novel type of aromaticity. *Nature* **181**, 1052–1053 (1958).

17. E. Heilbronner, Hückel molecular orbitals of Möbius-type conformations of annulenes. *Tetrahedron Lett.* **5**, 1923–1928 (1964).

18. M. Mauksch, V. Gogonea, H. Jiao, P. R. Schleyer, Monocyclic $(CH)_9^+$—A heilbronner Möbius aromatic system revealed. *Angew. Chem. Int. Ed.* **37**, 2395–2397 (1998).

19. D. Ajami, O. Oeckler, A. Simon, R. Herges, Synthesis of a Möbius aromatic hydrocarbon. *Nature* **426**, 819–821 (2003).

20. H. S. Rzepa, Möbius aromaticity and delocalization. *Chem. Rev.* **105**, 3697–3715 (2005).

21. R. Herges, Topology in chemistry: Designing Möbius molecules. *Chem. Rev.* **106**, 4820–4842 (2006).

22. R. Herges, Organic chemistry: Aromatics with a twist. *Nature* **450**, 36–37 (2007).

23. G. R. Schaller, F. Topić, K. Rissanen, Y. Okamoto, J. Shen, R. Herges, Design and synthesis of the first triply twisted Möbius annulene. *Nat. Chem.* **6**, 608–613 (2014).

24. M. Albrecht, G. van Koten, Platinum group organometallics based on "pincer" complexes: Sensors, switches, and catalysts. *Angew. Chem. Int. Ed.* **40**, 3750–3781 (2001).

25. H. A. Younus, W. Su, N. Ahmad, S. Chen, F. Verpoort, Ruthenium pincer complexes: Synthesis and catalytic applications. *Adv. Synth. Catal.* **357**, 283–330 (2015).

26. C. S. Wannere, D. Moran, N. L. Allinger, B. A. Hess Jr., L. J. Schaad, P. R. Schleyer, On the stability of large [4n]annulenes. *Org. Lett.* **5**, 2983–2986 (2003).

27. M. Mauksch, S. B. Tsogoeva, Demonstration of "Möbius" aromaticity in planar metallacycles. *Chemistry* **16**, 7843–7851 (2010).

28. R. Herges, D. Geuenich, Delocalization of electrons in molecules. *J. Phys. Chem. A* **105**, 3214–3220 (2001).

29. P. R. Schleyer, C. Maerker, A. Dransfeld, H. Jiao, N. J. R. van Eikema Hommes, Nucleus-independent chemical shifts: A simple and efficient aromaticity probe. *J. Am. Chem. Soc.* **118**, 6317–6318 (1996).

30. E. D. Glendening, J. K. Badenhoop, A. E. Reed, J. E. Carpenter, J. A. Bohmann, C. M. Morales, F. Weinhold, *NBO 5.0* (Theoretical Chemistry Institute, University of Wisconsin, Madison, 2001).

31. J. T. Robinson, S. M. Tabakman, Y. Liang, H. Wang, H. S. Casalongue, D. Vinh, H. Dai, Ultrasmall reduced graphene oxide with high near-infrared absorbance for photothermal therapy. *J. Am. Chem. Soc.* **133**, 6825–6831 (2011).

32. H. Cabral, Y. Matsumoto, K. Mizuno, Q. Chen, M. Murakami, M. Kimura, Y. Terada, M. R. Kano, K. Miyazono, M. Uesaka, N. Nishiyama, K. Kataoka, Accumulation of sub-100 nm polymeric micelles in poorly permeable tumours depends on size. *Nat. Nanotechnol.* **6**, 815–823 (2011).

33. M. Murakami, H. Cabral, Y. Matsumoto, S. Wu, M. R. Kano, T. Yamori, N. Nishiyama, K. Kataoka, Improving drug potency and efficacy by nanocarrier-mediated subcellular targeting. *Sci. Transl. Med.* **3**, 64ra2 (2011).

34. D. Peer, J. M. Karp, S. Hong, O. C. Farokhzad, R. Margalit, R. Langer, Nanocarriers as an emerging platform for cancer therapy. *Nat. Nanotechnol.* **2**, 751–760 (2007).

35. G. Liu, Z. Wang, J. Lu, C. Xia, F. Gao, Q. Gong, B. Song, X. Zhao, X. Shuai, H. Ai, Z. Gu, Low molecular weight alkyl-polycation wrapped magnetite nanoparticle clusters as MRI probes for stem cell labeling and in vivo imaging. *Biomaterials* **32**, 528–537 (2011).

36. G. Liu, J. Xie, F. Zhang, Z. Wang, K. Luo, L. Zhu, Q. Quan, G. Niu, S. Lee, H. Ai, X. Chen, N-Alkyl-PEI-functionalized iron oxide nanoclusters for efficient siRNA delivery. *Small* **7**, 2742–2749 (2011).

37. Y. Li, T.-y. Lin, Y. Luo, Q. Liu, W. Xiao, W. Guo, D. Lac, H. Zhang, C. Feng, S. Wachsmann-Hogiu, J. H. Walton, S. R. Cherry, D. J. Rowland, D. Kukis, C. Pan, K.S. Lam, A smart and versatile theranostic nanomedicine platform based on nanoporphyrin. *Nat. Commun.* **5**, 4712 (2014).

38. R. Singh, S. V. Torti, Carbon nanotubes in hyperthermia therapy. *Adv. Drug Deliv. Rev.* **65**, 2045–2060 (2013).

39. X. Ai, C. J. H. Ho, J. Aw, A. B. E. Attia, J. Mu, Y. Wang, X. Wang, Y. Wang, X. Liu, H. Chen, M. Gao, X. Chen, E. K. L. Yeow, G. Liu, M. Olivo, B. Xing, In vivo covalent cross-linking of photon-converted rare-earth nanostructures for tumour localization and theranostics. *Nat. Commun.* **7**, 10432 (2016).

40. R. He, Y.-C. Wang, X. Wang, Z. Wang, G. Liu, W. Zhou, L. Wen, Q. Li, X. Wang, X. Chen, J. Zeng, J. G. Hou, Facile synthesis of pentacle gold–copper alloy nanocrystals and their plasmonic and catalytic properties. *Nat. Commun.* **5**, 4327 (2014).

41. G. M. Sheldrick, *SADABS, Program for Semi-Empirical Absorption Correction* (University of Göttingen, Göttingen, Germany, 1997).

42. G. M. Sheldrick, *SHELXTL* (Siemens Analytical X-ray Systems, Madison, WI, USA).

43. A. D. Becke, Density-functional thermochemistry. III. The role of exact exchange. *J. Chem. Phys.* **98**, 5648–5652 (1993).

44. B. Miehlich, A. Savin, H. Stoll, H. Preuss, Results obtained with the correlation energy density functionals of Becke and Lee, Yang and Parr. *Chem. Phys. Lett.* **157**, 200–206 (1989).

45. C. Lee, W. Yang, R. G. Parr, Development of the Colle-Salvetti correlation-energy formula into a functional of the electron density. *Phys. Rev. B* **37**, 785–789 (1988).

46. P. J. Hay, W. R. Wadt, Ab initio effective core potentials for molecular calculations. Potentials for K to Au including the outermost core orbitals. *J. Chem. Phys.* **82**, 299–310 (1985).

47. S. Huzinaga, *Gaussian Basis Sets for Molecular Calculations* (Elsevier, Amsterdam, 1984).

48. M. J. Frisch, G. W. Trucks, H. B. Schlegel, G. E. Scuseria, M. A. Robb, J. R. Cheeseman, G. Scalmani, V. Barone, B. Mennucci, G. A. Petersson, H. Nakatsuji, M. Caricato, X. Li, H. P. Hratchian, A. F. Izmaylov, J. Bloino, G. Zheng, J. L. Sonnenberg, M. Hada, M. Ehara, K. Toyota, R. Fukuda, J. Hasegawa, M. Ishida, T. Nakajima, Y. Honda, O. Kitao, H. Nakai, T. Vreven, J. A. Montgomery Jr., J. E. Peralta, F. Ogliaro, M. Bearpark, J. J. Heyd, E. Brothers, K. N. Kudin, V. N. Staroverov, R. Kobayashi, J. Normand, K. Raghavachari, A. Rendell, J. C. Burant, S. S. Iyengar, J. Tomasi, M. Cossi, N. Rega, J. M. Millam, M. Klene, J. E. Knox, J. B. Cross, V. Bakken, C. Adamo, J. Jaramillo, R. Gomperts, R. E. Stratmann, O. Yazyev, A. J. Austin, R. Cammi, C. Pomelli, J. W. Ochterski, R. L. Martin, K. Morokuma, V. G. Zakrzewski, G. A. Voth, P. Salvador, J. J. Dannenberg, S. Dapprich, A. D. Daniels, Ö. Farkas, J. B. Foresman, J. V. Ortiz, J. Cioslowski, D. J. Fox, *Gaussian 09, Revision D. 01* (Gaussian Inc., Wallingford, CT, 2013).

49. A. D. Becke, Density-functional exchange-energy approximation with correct asymptotic-behavior. *Phys. Rev. A* **38**, 3098–3100 (1988).

50. J. B. Foresman, T. A. Keith, K. B. Wiberg, J. Snoonian, M. J. Frisch, Solvent effects. 5. Influence of cavity shape, truncation of electrostatics, and electron correlation on ab initio reaction field calculations. *J. Phys. Chem.* **100**, 16098–16104 (1996).

The following resources related to this article are available online at
http://advances.sciencemag.org. (This information is current as of September 4, 2016):

Updated information and services, including high-resolution figures, can be found in the online version of this article at:
http://advances.sciencemag.org/content/2/8/e1601031.full

Supporting Online Material can be found at:
http://advances.sciencemag.org/content/suppl/2016/08/22/2.8.e1601031.DC1

This article **cites 44 articles,** 2 of which you can access for free at:
http://advances.sciencemag.org/content/2/8/e1601031#BIBL